Title
Oxygen redox activities governing high-voltage charging reversibility of Ni-rich layered cathodes

Journal
Energy & Environmental Science, 17(23)

ISSN
1754-5692

Authors
Lee, Gi-Hyeok
Lee, Suwon
Zhang, Jiliang
et al.

Publication Date
2024-11-26

DOI
10.1039/d4ee03832k

Oxygen Activities Governing Structural Reversibility in Industrial Ni-Rich Layered Cathodes

Gi-Hyeok Lee,[1] Suwon Lee,[2] Jiliang Zhang,[3] Bernardine L. D. Rinkel,[4] Matthew J. Crafton,[4,5] Zengqing Zhuo,[1] Youngju Choi,[2] Junghoon Yang,[6] Jongwook W. Heo,[7] Byungchun Park,[7] Bryan D. McCloskey,[4,5] Maxim Avdeev,[8,9] Wanli Yang,[1,*] Yong-Mook Kang[2,10,11,*]

[1]Advanced Light Source, Lawrence Berkeley National Laboratory, Berkeley, CA, USA

[2]Department of Materials Science and Engineering, Korea University, Seoul, Republic of Korea

[3]School of Materials Science and Engineering, Dalian Jiaotong University, Dalian, Liaoning, PR China

[4]Energy Storage and Distributed Resources Division, Lawrence Berkeley National Laboratory, Berkeley, CA, USA

[5]Department of Chemical and Biomolecular Engineering, University of California, Berkeley, CA, USA

[6]Carbon Materials Application Research Group, Korea Institute of Industrial Technology, Jeonju, Jeollabuk-do, Republic of Korea

[7]Advanced Cell Research Center, LG Energy Solution, Daejeon, Republic of Korea

[8]Australian Nuclear Science and Technology Organization, Lucas Heights, New South Wales, Australia

[9]School of Chemistry, The University of Sydney, Sydney, New South Wales, Australia

[10]Department of Battery-Smart Factory, Korea University, Seoul, Republic of Korea

[11]KU-KIST Graduate School of Converging Science and Technology, Korea University, Seoul, Republic of Korea

Abstract

The chemical reactions and phase transitions at high voltages determine the electrochemical properties of high voltage layered cathodes such as Ni-rich rhombohedral materials. Here, we performed a comprehensive and comparative study of the cationic and anionic redox reactions, as well as the structural evolution of a series of industrial Ni-rich layered cathode materials with and without Al doping, which are being utilized in the cells made by LG Energy Solutions Co.. We combined the results from X-ray spectroscopy, operando electrochemical mass spectrometry, and neutron diffraction with electrochemical properties, and revealed the different oxygen activities associated with structural and electrochemical degradations. We show that Al doping suppresses

the irreversible oxygen release thereby enhancing the reversible lattice oxygen redox resulting from the interplay between static (doped Al) and dynamic disorders (reversible oxygen redox). With this modulated oxygen activity, the Ni-rich cathode's notorious H2-H3 structural phase transition becomes highly reversible. Our findings disentangle the different oxygen activities during high-voltage cycling and clarify the role of dopants in the Ni-rich layered cathodes in terms of structural and electrochemical stability finally making all the cell makers get back to the fundamental investigation regarding whether high-Ni NCM chemistry (NCM811 or NCM 91/2 1/2) is substantially beneficial compared to its mid-Ni homologues (NCM622).

Main

In Ni-rich $LiNi_xCo_yMn_{1-x-y}O_2$ (NR-NCMs), most lithium-ion extraction occurs in a voltage range that does not deviate from the chemical window of the electrolyte, due to the relatively low redox potential of $Ni^{2+/3+/4+}$.[1] Increasing the Ni content of NCMs allows to access higher capacity by avoiding excessive electrolyte decomposition that can deteriorate the cell performance. [2-4] However, the increased Ni content significantly worsens the structural and thermal stability of the layered cathode materials and intensifies accompanying parasitic reactions such as cracking, gas evolution, and surface degradation. [5-8] The degradation of NR-NCMs is typically accompanied by oxygen deficiency resulting from the formation of oxygen-deficient phases coupled with the release of oxygen-containing gases. Thus, the origin leading to oxygen loss might be primarily responsible for the overall deterioration of the layered cathodes. Traditionally, surface oxygen loss has been mainly attributed to electrolyte decomposition reactions. [9-11] On the other hand, oxygen redox reactions have been shown to also occur in most of layered cathodes utilizing non-alkali rich chemistry, including rhombohedral symmetry-based cathodes like NR-NCMs. [12-20] Compared with

transition metal (TM) redox centers, the involvement of oxygen redox reactions often activates irreversible reactions such as oxygen loss. Moreover, the increased Ni content in NCMs and the resulting active formation of NiO could render the charging reaction to be completely irreversible depending on its chemical composition. Therefore, understanding the oxygen activities within NR-NCMs and the relationship between oxygen redox and parasitic reactions looks crucial in providing a clear design direction for the stabilization of NR-NCMs.

The extensive efforts during the last decade for investigating the fundamental mechanism and practical route to utilize the optimal oxygen redox reactions have witnessed the power of two particular techniques directly associated with oxygen activities: operando electrochemical mass spectrometry (OEMS) and resonant inelastic X-ray scattering (RIXS). [12,21-25] OEMS detects the different forms of oxygen release, including oxygen and other gas release made from radical oxygen. [23,26-28] It helps to detect the irreversible oxygen activities that often occur through oxygen oxidation at high voltages. On the other hand, RIXS has been established for probing the oxidized oxygen species, which remain stable in the lattice, i.e., without release, through spectroscopic fingerprints of oxidized oxygen. [17,29-32]

So, here, we studied a series of NR-NCMs industrially employed in electric vehicles by correlating OEMS and mapping of RIXS (mRIXS), with other structural and electrochemical characterizations. Unexpectedly, the mRIXS results displayed an absence of lattice oxygen redox features, even though Li-stoichiometric layered oxides in non-Ni-rich compositions typically exhibited such features. [15,33-36] By contrast, when incorporating a minor quantity of Al dopant into NR-NCMs (NR-NCMAs), oxygen redox features were evidentially revived. The oxygen evolution behaviors of NR-NCMs and NR-NCMAs observed through OEMS clearly demonstrate that the oxygen redox or activity of NR-NCMS is unstable resultantly leading to serious oxygen gas

evolution, while that of NR-NCMAs looks stabilized only with a minimal amount of oxygen evolution. More importantly, in concert with the different oxygen activities in NR-NCMs and NR-NCMAs, we found the reversibility of the notorious H2-H3 phase transition in NR-NCMs got greatly improved thanks to the stabilized oxygen activity Al doping. The combination of our results suggests that the H2-H3 phase transition itself may not be the culprit responsible for the parasitic degradation of NR-NCMs, and instead controlling the oxygen activities of NR-NCMs at high voltages is critical for improving its structural and electrochemical stability.

Structural and electrochemical properties of NR-NCMs

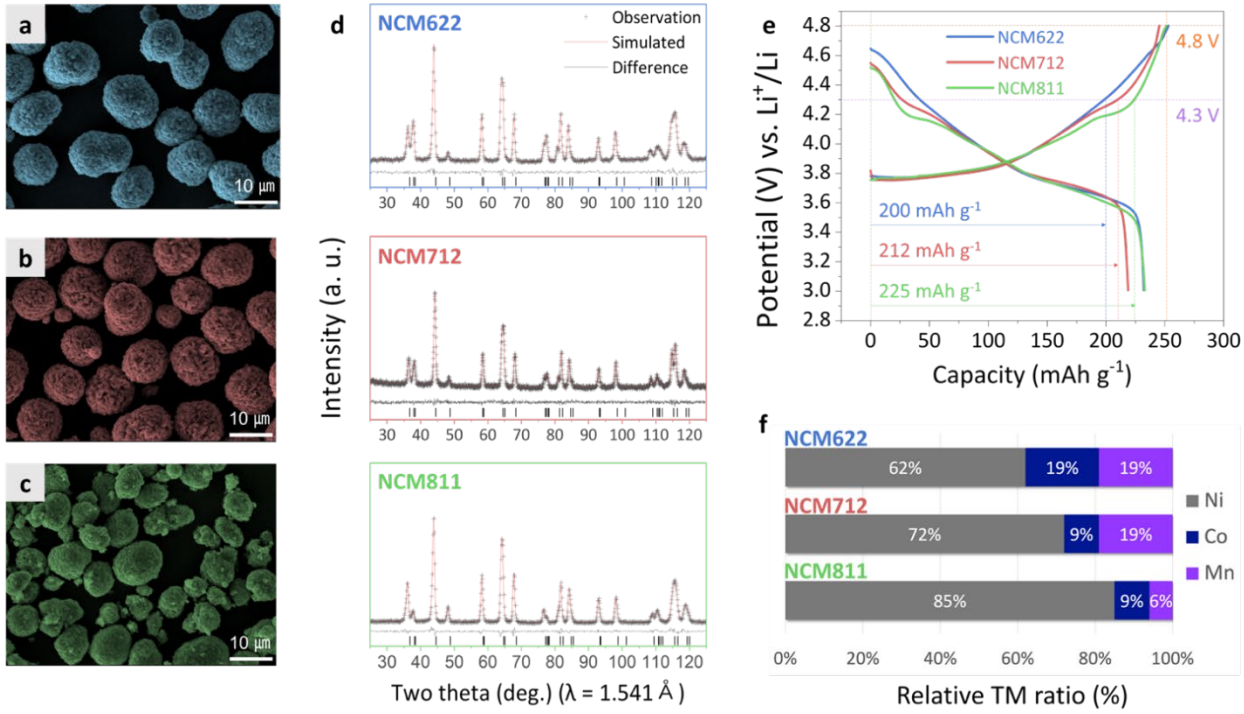

Figure 1. Physicochemical properties of pristine NR-NCMs. **a-c** Scanning electron microscopy (SEM) images of NCM622 (blue), NCM712 (pink), and NCM811 (green). **d** Neutron diffraction patterns and fitted results of NCM622, NCM712, and NCM811. **e** Galvanostatic voltage profiles of NCM622, NCM712, and NCM811 for the first cycle. **f** Elemental composition of TMs in NR-NCMs based on the ICP-OES results (**Table S1**).

The materials used in this study are industrial NR-NCMs (LG Energy Solution) that have strictly similar physicochemical properties and manufacturing processes between samples. See **Table S1** for the exact elemental composition of the cathodes. **Fig. 1** shows the structural and electrochemical properties of the pristine NR-NCMs, including morphologies, crystallinity, and elemental compositions. All NR-NCMs show similar spherical morphologies in 100 nm-sized primary particles. The neutron diffraction (ND) patterns of the pristine electrodes show narrow full width at half maximum (FWHM) reflection peaks and do not show any scattering peaks other than the $R\bar{3}m$ symmetry. This indicates that the NR-NCMs exhibit high purity and crystallinity. In addition, ND has higher sensitivity to light elements like Li than X-ray diffraction (XRD) due to

the larger scattering cross-section, which helps with accurate Li/Ni anti-site defect quantification. **Table S2** shows the results of Rietveld refinement of the NR-NCM ND patterns, indicating a limited number of Li/Ni anti-site defects.

The NR-NCMs show capacities of 250 mAh g^{-1} in the first charging process under 4.8 V cut-off conditions, meaning that most of the Li ions have been extracted (~93 % vs. theoretical capacity). The shape of the voltage profile is consistent with the shape of previously reported NR-NCMs, and the plateau for the H2-H3 phase transition that occurs characteristically at ~4.2 V is also clearly shown for NCM712 and NCM811. The 4.2 V plateau has been reported to strengthen as the Ni content increases to Ni 70%, and **Fig. 1e** also shows that the plateau elongates with higher Ni content in NR-NCMs. [4]

Redox behavior of NR-NCMs

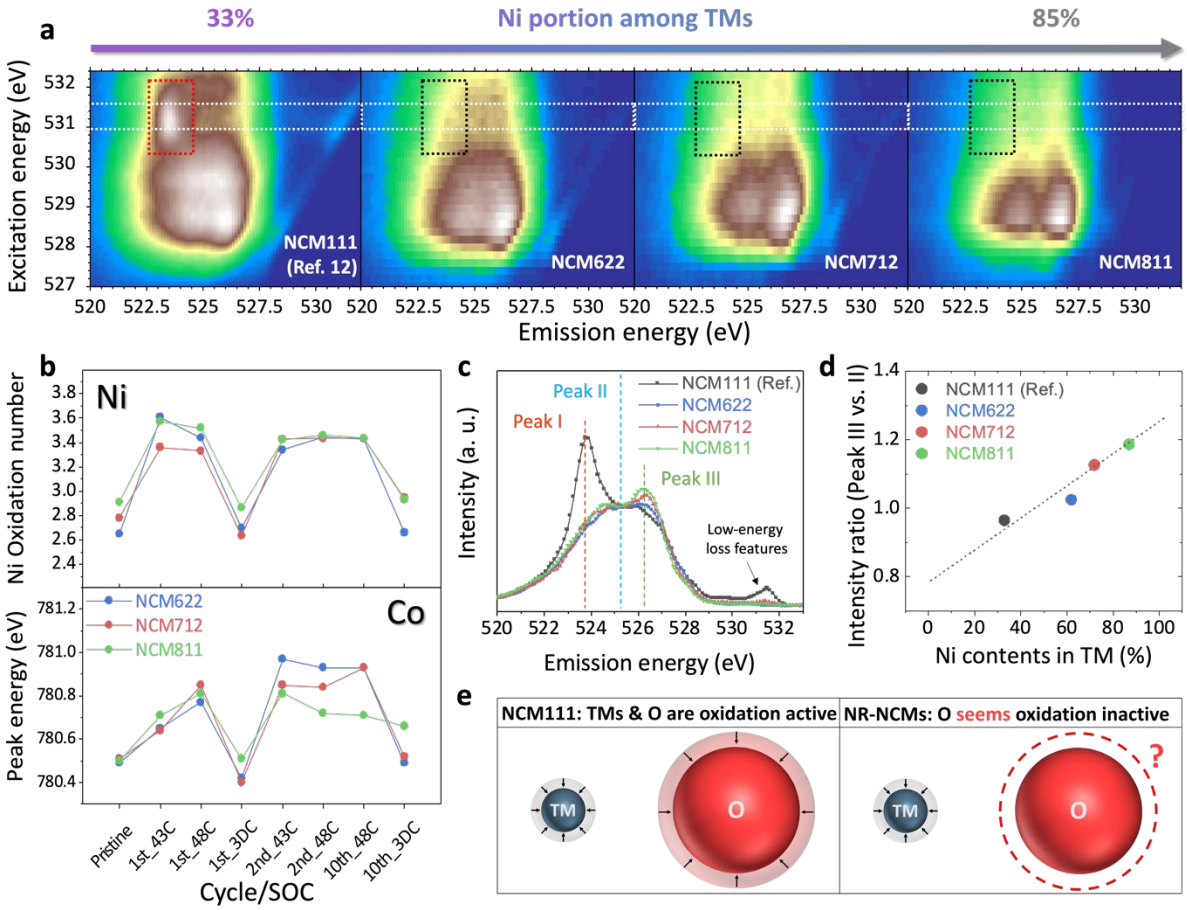

Figure 2. a mRIXS spectra of 4.8 V charged $LiNi_{0.33}Co_{0.33}Mn_{0.33}O_2$ (NCM111) and NR-NCMs. [12] Reproduced with permission. Copyright 2020, Wiley. **b** Redox trend of Ni and Co based on the sXAS spectra of L_3-edges. sXAS spectra of Ni & Co L_3-edges were collected using TFY mode (**Fig. S1** and **S2**). Semi-quantitatively fitted Ni oxidation state trends were extracted from the Ni-L_3 spectra. The fitted value was generated by the linear combination of the simulated $Ni^{2+/3+/4+}$ spectra plotted at the bottom of the boxes (Upper panel). Co peak energy trends during the cycling, extracted from the Co L_3-edge spectra (Lower panel). **c** Integrated RIXS cuts extracted from the white dotted boxes in **Fig. 3a**. **d** The Peak III vs. II trend as a function of Ni content in NR-NCMs. The dotted trendline in the panel shows a linear correlation that depends on the NCM Ni content. **e** An illustration of the contrast in redox centers between NCM111 and NR-NCMs.

Many studies of Li-stoichiometric rhombohedral cathodes ($LiTMO_2$) have suggested a contribution of oxygen in charge compensation, and mRIXS has experimentally revealed the existence of oxidized oxygen in the cathodes. [12,16,21,31] Although the TM dependency of the oxygen redox behavior is still elusive, [25,37] mRIXS has been established as the tool to detect the oxidized

oxygen, at least in states with O-O bonding, e.g., peroxo- or O_2, [38,39] through two fingerprinting features at 531 eV excitation energy, one at about 523.7 eV emission energy, the other close to the elastic peak (NCM111 in **Fig. 2a**). [25,30, 32]

The O-*K* mRIXS spectrum of the 3d TM-based cathode material shows two types of peaks in the range 527–532 eV. As shown in our previous reports on oxygen redox activity for fully charged NCM111, presented in Fig. 2a, there is a peak with a broad emission energy width near the excitation energy of about 528–531 eV originated by TM-O hybridization. [40] The other feature appears at an excitation energy of 531.2 eV (red dotted box in Fig. 2a), which has been considered a peak related to O-O bonding formation from oxygen redox. [12,17,25,32] Additionally, low-energy loss features close to the elastic peak always appear together with the aforementioned feature. [29,30] Fig. 2a shows mRIXS spectra of NR-NCMs fully charged to 4.8 V, along with the previously reported NCM111. [12] In sharp contrast with NCM111, no oxygen redox features are found in NR-NCMs, as shown in the area indicated by the dotted box. **Fig. 2c** further clarifies by showing the integration of RIXS intensity within the excitation range indicated by the white dotted boxes in Fig. 2a. For a direct comparison, these integrated RIXS intensities are normalized based on the intensity of Peak II, and important peaks are classified into Peak I, Peak III, and low-energy loss features with the elastic peak. A strong Peak I is observed in only NCM 111, which represents oxidized lattice oxygen. [12] Additionally, the low-energy loss feature close to the elastic peak gets strongly enhanced, as mentioned above. In sharp contrast, none of the NR-NCMs display clear signatures of such oxidized oxygen states, indicating a negligible amount of oxidized oxygen detected by RIXS.

The origin of Peak III has been observed in Ni systems before but has not been understood. [16,22] In **Fig. 2d**, the Peak III vs. II values of fully charged NR-NCMs are plotted against Ni content, and

the intensities show a linear correlation. Since the 4+ oxidation state of Ni is dominant in NR-NCMs in the fully charged state, the corresponding intensity is presumably due to the increase in Ni^{4+} content. Therefore, our comparative study here finally clarifies that Peak III stems from the nominal Ni^{4+} state hybridized with O.

Fig. 2b and **S3a** show the quantification results of the oxidation number of Ni through the semi-quantitative fitting of the Ni-L_3 total fluorescence yield (TFY) and total electron yield (TEY) soft X-ray absorption spectroscopy (sXAS) spectra (**Fig. S1** and **S3**). Transition metal *L*-edge spectroscopy directly probes 3d orbitals by utilizing the 2p to 3d transition of a 3d TM. [32,40-44] In particular, various transition metals, including Ni and Mn, have unique absorption spectral shapes for each oxidation number, as shown in the box in **Fig. S1** and **S3**, which enables semi-quantitative fitting. [12,45-47] TFY and TEY modes have detection limits of up to 200 nm and 10 nm depth from the surface, respectively. Therefore, the difference in materials between the surface and the relative bulk can be compared by comparing the spectra obtained in the two modes. [48]

Once NR-NCMs are charged up to 4.3 V in the first charge, an increase in the oxidation number of Ni is observed in both the TEY and TFY. In subsequent charging, upon 4.8 V in all three samples, the TFY oxidation number tends to be reduced compared to the number when the SOC was 4.3 V. For TEY results, the oxidation slows down or is more reduced at the SOC of 4.8 V compared to 4.3 V, as the Ni content of the NR-NCM increases. In general, the reduction of the oxidation number of Ni in the charging process indicates the loss of oxygen. As a result, it irreversibly forms a relatively oxygen-deficient phase and reduces the total amount of available lithium during the discharge process, which is a cause of cycle decay. For all samples, the SOC at 4.3 V increases as the Ni content in NR-NCMs increases. Therefore, relatively more oxidation of redox centers at 4.3 V is expected for NCM811 than NCM712 and NCM622. Likewise, during the initial charging

process, Ni is shown to undergo irreversible oxidation, both on the surface and in the bulk. After the second cycle, the oxidation number on the surface at 4.8 V is significantly increased compared to at 4.3 V, and the oxidation number is decreased in the fully charged state of the tenth cycle, indicating the oxygen loss is reduced upon extended cycling. On the other hand, in the second cycle, the bulk-sensitive TFY data show that NCM712 and NCM811 slightly increased oxidation number at 4.8 V compared to 4.3 V. The oxidation number of Ni in the fully charged state of the tenth cycle, compared to the second cycle, decreased slightly for NCM811 and showed similar levels for NCM622 and NCM712. In the NR-NCMs, Mn exists as 4+ in all SOCs (**Fig. S5**). Ni is a dominant contributor to redox up to 4.3 V, and Co acts as an active redox center over the entire redox range. Since there is a redox center that can be qualitatively explained for all sections, the redox behavior of NCMs has been understood to come from the TM centers. The observation of the redox trends of TMs in NR-NCMs corresponds well with previous reports. [49-52]

Based on the oxidation behavior of redox centers in NCMs shown in Fig. 2, cationic redox is dominant in NR-NCMs, and it seems that oxygen redox hardly occurs, or at least cannot be detected by RIXS as in NCM111. However, this conclusion contrasts with the strong oxygen redox peak found in other Li-stoichiometric layered oxide cathodes, such as LCO, NCM111, $LiNi_{0.85}Co_{0.10}Al_{0.05}O_2$ (NCA), and $LiNiO_2$ (LNO). [12,16-18] Strong oxygen redox features found in the rhombohedral cathodes with various chemical compositions impose difficulties in the interpretation of the oxygen redox behaviors in Fig. 2 for the following reasons: (1) Despite the same symmetry and Li content, only NR-NCMs do not show strong oxygen redox features at high voltages. (2) Oxygen redox features were found even in cathodes with relatively high (NCA and LNO) or low (LCO and NCM111) Ni content. This non-linearity suggests that mRIXS does not reflect the total oxidation amount of lattice oxygen. The observations of oxygen redox feature

through mRIXS do not include oxygen species that are irreversibly lost during oxidation. Therefore, the absence of an oxygen redox feature in RIXS could have two contrary possibilities: (1) The lattice oxygen is not oxidized; (2) The oxidized-oxygen species are lost through mechanisms such as gas evolution.

The contrast in oxygen redox peak intensities from Al-doped NR-NCMs (NR-NCMAs)

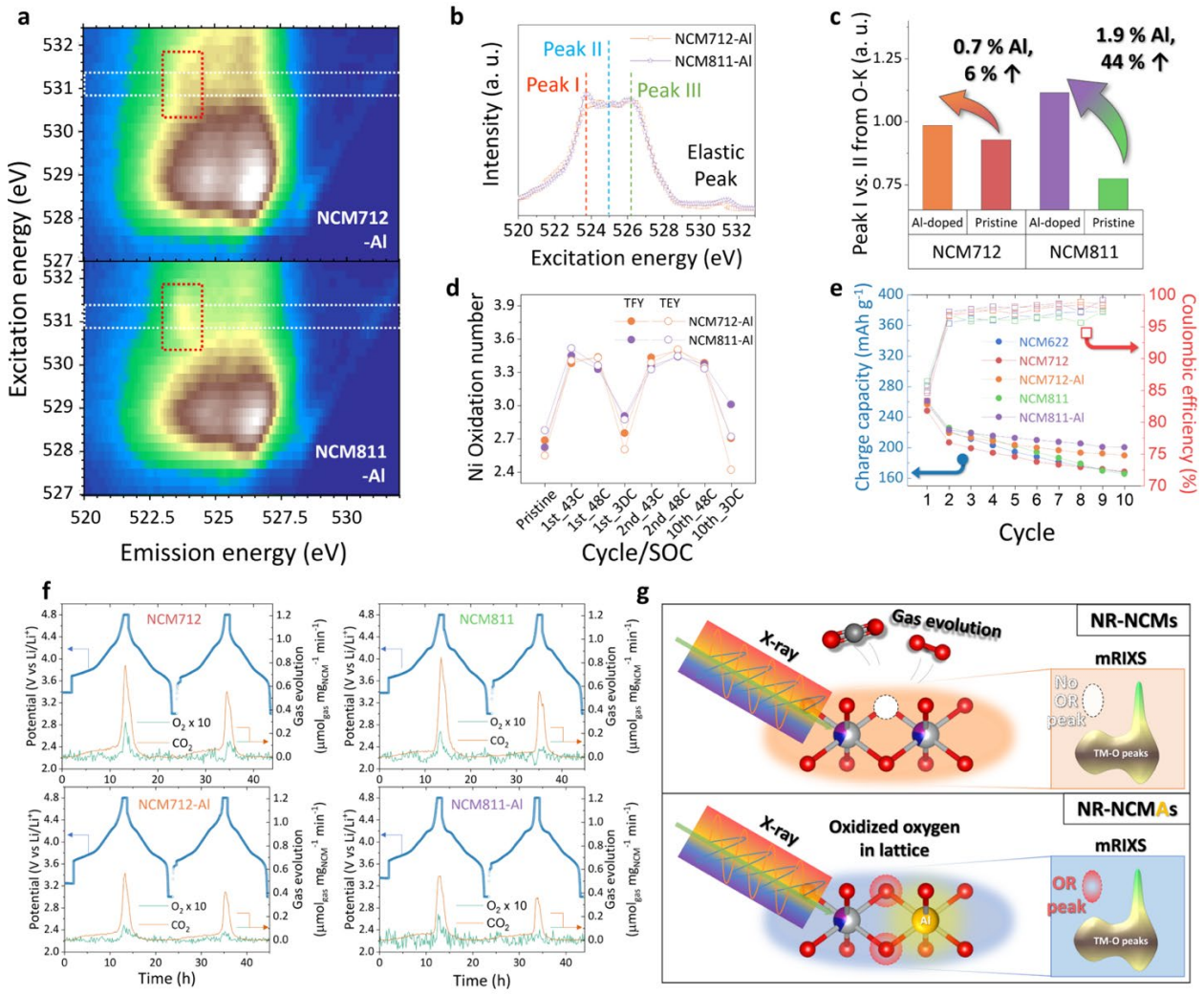

Figure 3. a-c Enhanced oxygen redox features of Al-doped NR-NCMs (NR-NCMAs). **a** mRIXS spectra of fully charged $LiNi_{0.72}Co_{0.09}Mn_{0.19}Al_{0.007}O_2$ (NCM712-Al) and $LiNi_{0.88}Co_{0.05}Mn_{0.07}Al_{0.019}O_2$ (NCM811-Al). **b** Integrated RIXS cuts extracted from the white dotted boxes in **Fig. 3a**. **c** Oxygen redox feature intensity (calculated by Peak I vs. II) comparison between Al-doped and pristine samples at a 4.8 V charged state. **d** Semi-quantitatively fitted Ni oxidation state trend extracted from Ni-L_3 TFY spectra. (**Fig. S7**) **e** Cyclability and coulombic efficiency comparison for NR-NCMs and NR-NCMAs. **f** OEMS results of NCM712, NCM712-Al, NCM811 and NCM811-Al. **g** An illustration of the reason for the contrast of oxygen redox features in NR-NCMs and NR-NCMAs. The irreversibly oxidized oxygen in NR-NCMs was not observed by RIXS, while the Al-stabilized oxidized oxygen was observed in NR-NCMAs.

When a specific amount of doping is performed on an NCM, the adjusted physicochemical properties of the cathodes improve the reversibility during cycling, as well as hysteresis, gas

evolution, thermal stability, and surface stability. [15,33,34] Al is one of the most representative dopants for NCMs, and it has been known to be effective in relieving the referred parasitic reactions. More specifically, it has been suggested that introducing Al positively affects oxygen redox, and there is some indirect evidence that oxygen redox is stabilized or generated. [15,33-36] The $LiNi_{0.72}Co_{0.09}Mn_{0.19}Al_{0.007}O_2$ (NCM712-Al; 0.7 at% Al vs. TMs) and $LiNi_{0.88}Co_{0.05}Mn_{0.07}Al_{0.019}O_2$ (NCM811-Al; 1.9 at% Al vs. TMs), hereafter named NR-NCMAs, used in our experiment were manufactured by the same industry supplier (LG Energy Solution), and were structurally almost identical to the NR-NCMs, except that they contained a small amount of Al. The small amount of doping does not significantly change the elemental composition of the NR-NCMs. [15,33,34]

Fig. 3a shows the mRIXS spectra of the fully charged NR-NCMAs in the first cycle. The summed RIXS cuts in **Fig. 3b** clearly reveal the occurrence of features regarding oxidized oxygen. In the spectrum from NCM811-Al, Peak I is a clear peak, and the same peak is shown as a shoulder for NCM712-Al, which has relatively low Al content. Although the Peak I intensity of NCM712-Al is relatively weak, there is a clear intensity enhancement compared to the summed RIXS cuts of NCM712 (Fig. 2c). **Fig. 3c** compares the relative intensities of Peak I vs. II between the NR-NCMs and NR-NCMAs. The increase of oxygen redox feature intensity through Al doping is clear, and the increment seems associated with the amount of Al. An important question is how the trace amounts of Al doping dramatically change oxygen activity.

Fig. 3f and **Table S3** present the OEMS results. The decrease in gas evolution after Al doping has been found to be consistent with the improved reversibility of Al-doped systems. The less oxygen evolution found in OEMS results and stronger oxygen redox intensity found in RIXS results of the NR-NCMAs, compared with NCMs, are very counterintuitive. Naively, Al tends to introduce a relatively more ionic environment for oxygen, which could be considered a factor that promotes

oxygen oxidation. However, our combined OEMS and RIXS results strongly suggest that Al doping in the NR-NCM system actually stabilizes oxygen oxidation, leading to less oxygen release but stronger lattice oxygen redox. A recent report from Oswald et al. based on OEMS claims that irreversible oxygen release from NR-NCMs at high SOC dominates the cycle stability. [53] In the cyclability results in **Fig. 3e**, NR-NCMs and NR-NCMAs, charged and discharged under the cut-off conditions of 3.0–4.8 V, both show a rapid capacity decrease during ten repeated cycles, but NR-NCMAs show a relatively slow capacity decay. This result is consistent with the scenario of the stabilization effect of Al doping. Based on the comprehensive analyses in Fig. 2 and 3, **Fig. 3g** illustrates the reason for the absence of oxygen redox peaks in NR-NCMs. While the NR-NCMs lose lattice oxygen in an irreversible oxidation environment, Al-stabilizes oxidized oxygen and suppresses oxygen release.

Reversibility of structural phase transformation through Al-doping

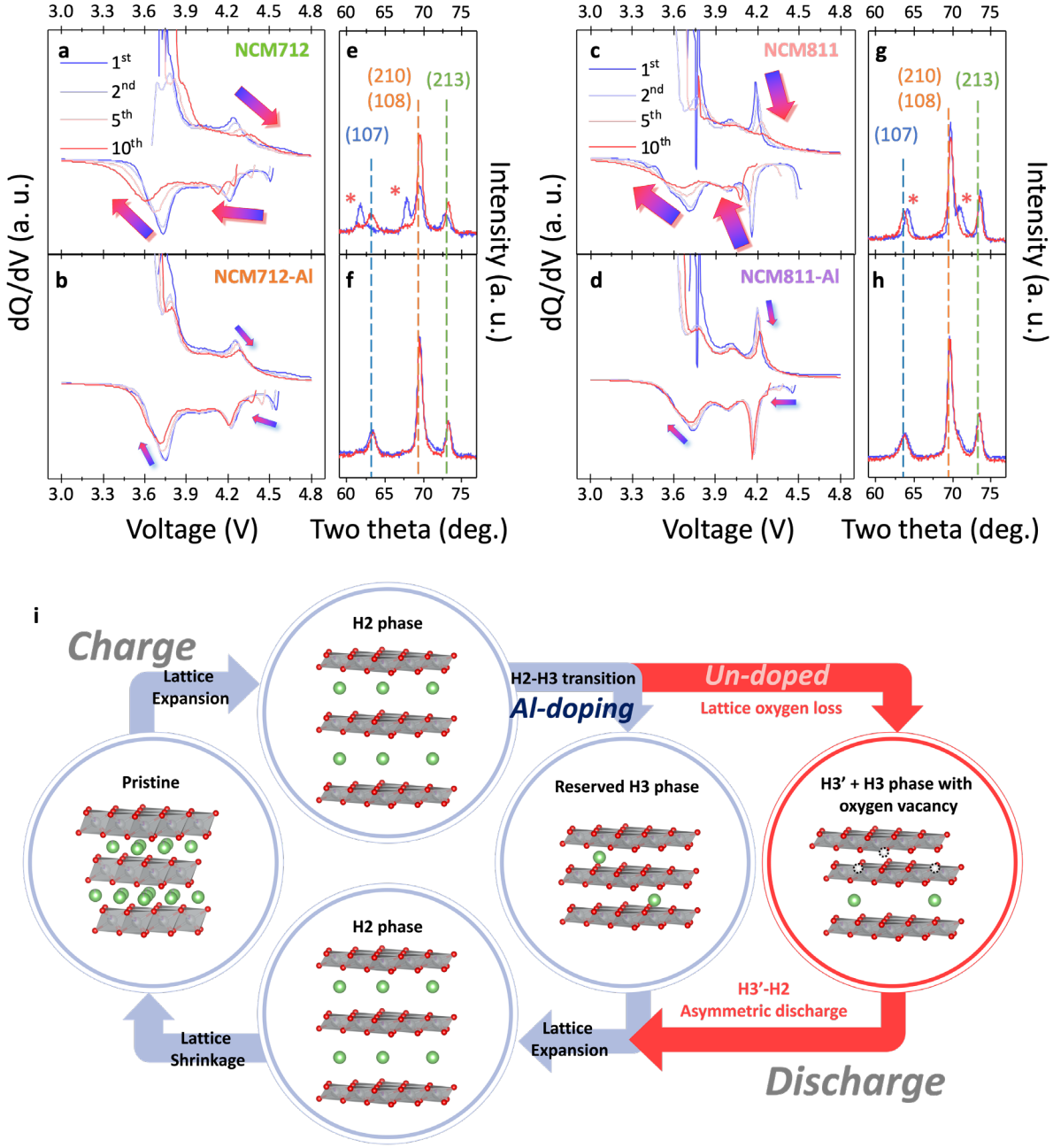

Figure 4. Electrochemical and structural contrasts after Al doping in NR-NCMs. **a-d** dQ/dV analyses results of **a, b** NCM712 and NCM712-Al and **c, d** NCM811 and NCM811-Al. **e-h** Neutron diffraction patterns of the fully charged NR-NCMs and NR-NCMAs collected with a wavelength of 1.541 Å. **e, f** NCM712 and NCM712-Al and **g, h** NCM811 and NCM811-Al. The patterns of the first and tenth cycles are plotted by blue and red solid lines, respectively. The reflections indicated by dashed lines are (107), (108), (210), and (213), which are the reflections of the R$\bar{3}$m space group. The asterisks highlight the unexpected additional phases. **i** A schematic illustration explaining the structural reversibility enhancement from stabilizing oxidized oxygen by Al doping.

It has been reported that the irreversible parasitic reactions are accompanied by oxygen redox at the high SoC of NR-NCMs. Hysteresis, cationic rearrangement, structural evolution, and oxygen gas evolution have been revealed through various methodologies, such as XRD/ND, X-ray absorption fine structure (XAFS), Raman spectroscopy, OEMS, and electron microscopy. [3,4,30,53-55] These irreversible behaviors start or show the most remarkable change around 75% SOC, where the H2-H3 phase transition occurs, which is considered the main cause of cycle degradation. These studies demonstrate that the occurrence of the H2-H3 phase transition depends more on the SOC than on the reaction potential. Interestingly, as shown in **Fig. S9** and **S10**, the oxygen redox in NR-NCMAs is also observed at a 4.3 V cut-off voltage. The oxygen redox in the Li-rich layered cathodes is often believed to occur around 4.5 V, as it indicates a distinct contrast in oxygen redox intensity before and after the long plateau near 4.5 V. However, it's worth noting that oxygen redox starts from around 4.3 V in NCM712-Al and NCM811-Al, which show stable oxygen redox behaviors through the fully charged state. The 4.3 V correspond to 78 % and 83 % SoC for NCM712-Al and NCM811-Al, respectively, which are immediately after 75 % of the H2-H3 phase transition. Thus, the oxygen redox demonstrating SoC dependence rather than being solely potential-driven adds another interesting similarity with the H2-H3 phase transition.

According to crystallographic analyses, the H2-H3 phase transition also leads to a sharp decrease in the c-lattice parameter of cathodes. Several factors, including oxygen oxidation, have also been considered to cause the H2-H3 phase transition. Saubanère et al. argue that interlayer O-O formation occurs when oxygen oxidation occurs in 3d metal Li-rich layered oxides due to the weakening of the repulsive force and the shortening of the distance between two TM-O slabs. [56] In addition, Zhang et al. argue that interlayer O-O formation may also occur in NCM, causing the H2-H3 phase transition. [5,57] Conversely, Liu et al. observed changes in detailed slab distance

according to SOC through ND. They claim that the decrease in slab distance at about 75% of SOC is due to the weakening of covalency by oxygen oxidation. [4] Similar slab changes were also observed by Lee et al., [3] and a decrease in covalency at high SOC was also observed by Raman spectroscopy by Flores et al. [53] Likewise, the correlation between the irreversible H2-H3 phase transition and the oxygen redox is still elusive, including their causality.

To further elucidate the correlation between the reversibility of oxygen oxidation and degradation behaviors, we perform ND and electrochemical analysis of the NR-NCMs and NR-NCMAs to reveal the degradation behaviors in terms of structural reversibility (**Fig. 4)**. **Fig. 4a-d** shows the dQ/dV results of NCM712/712-Al and NCM811/811-Al. In **Fig. 4a**, the intensity of the NCM712 H2-H3 peak around 4.2 V significantly decreases, with a large peak broadening through ten cycles, and the peak position shifts to a higher voltage. NCM811 (**Fig. 4c**) shows more dramatic changes due to the higher Ni content. The H2-H3 transition peak gets diminished, and a slight peak shift occurs after ten cycles. Similar changes in dQ/dV peaks are also observed during the discharging process: peak intensity decay, shifts, and broadenings are also observed around 4.2, 4.0, and 3.7 V. On the other hand, in NR-NCMAs, these changes are significantly alleviated.

Fig. 4e-h, which compares the ND patterns of the first and tenth cycles, shows the initial irreversible structural evolution of NR-NCMs. For NR-NCMs, in addition to the (107), (108), (210), and (213) diffraction peaks highlighted by dashed lines, additional peaks, indicated by asterisks, occur. As reported by Liu et al., the four diffraction peaks for r-3m symmetry are monotonically shifted to a higher degree from their original position in pristine NCMs, and the additional peaks have not been observed for pristine NCMs. [4] **Fig. S11** shows ND patterns over the full two-theta range (25–120˚), supporting the structural hysteresis. Each additional peak appears at an angle that is a certain level away from each diffraction peak, presumably from the

phase separation. In the case of NCM712, the new peak occurs on the lower angle of the three diffraction peaks. On the other hand, in NCM811, an additional peak is observed to occur at a higher angle than the peaks. Interestingly, after this peak is found in the first cycle, it is found to be very weak upon reaching the tenth cycle. In sharp contrast, the ND patterns of the first and tenth cycles are very similar in NR-NCMAs. The limited phase separation of NCM811-Al supports the structural reversibility enhancement by Al doping.

As combined OEMS and RIXS results discussed earlier, the ND results clarify that the lattice oxygen redox itself is not necessarily responsible for the irreversibility of the structural phase transition. The observation of the stronger lattice oxygen redox features in NR-NCMAs, compared with NR-NCMs, indicates that controlled oxygen oxidation is not the culprit of irreversible behaviors in electrochemistry and structure.

Conclusions

A comparative study of a series of industrial NR-NCMs and NR-NCMAs with different compositions shows that the oxygen activities of Ni-rich layered materials determine their structural and electrochemical degradation phenomena, especially at high voltages. These industrial NR-NCMs display negligible lattice oxygen redox features in their mRIXS spectra while showing strong oxygen gas release through OEMS. Interestingly, introducing a trace amount of Al (0.7-1.9 at%) into NR-NCMs activates a clear lattice oxygen redox feature in the mRIXS spectra while significantly suppressing the oxygen gas release during OEMS. A comparative in situ structural investigation between NR-NCMs and NR-NCMAs also demonstrates a stark contrast in the H2-H3 phase transition behavior, with the Al dopant playing a key role in enhancing its structural reversibility and electrochemical cyclability during the extended cycling. The

observation on stable or unstable oxygen redoxes through mRIXS combined with OEMS probing oxygen release behavior suggests that controlling the oxygen activities of NR-NCMs at high voltages plays a pivotal role to improve the structural reversibility through controlling the parasitic H2-H3 phase transition and so on, which is achievable through elemental doping and critical for improving the electrochemical performances of Li-stoichiometric layered cathodes. This discovery made a significant milestone which rendered all the battery industry to not only reconsider mid-Ni NCMs away from sticking to developing the potentially unstable NCMs with above 80% of Ni but also understand why NCMAs should be advantageous compared with NCMs in every aspect.

Acknowledgments

This work was supported by the National Research Foundation of Korea (NRF) grant funded by the Korea government (MSIT) (NRF-2022R1A2B5B03001781) and the Nano & Material Technology Development Program through the National Research Foundation of Korea(NRF) funded by Ministry of Science and ICT(RS-2023-00282389). YMK acknowledges the financial support from LG Energy Solution. Co., LTD. GHL and WY thank the partial support of the U.S. DOE Office of Science, Scientific User Facilities project titled “Integrated Platform for Multimodal Data Capture, Exploration, and Discovery Driven by AI Tools. Soft X-ray experiments were performed at BL8.0.1 of the Advanced Light Source (ALS), a DOE Office of Science User Facility, under contract no. DE-AC02-05CH11231.

Methods

General characterizations (ICP-AES, XRD, ND, SEM)

All cathode materials (NCM622, NCM712, NCM712-Al, NCM811, NCM811-Al) used in this work are provided by LG Energy Solution. The ICP-AES results were collected with a PerkinElmer OPTIMA 8300 ICP mass spectrometer installed at the National Center for Inter-university Research Facilities (NCIRF) at Seoul National University. X-ray diffraction (XRD) patterns were collected by Rigaku Smartlab X-ray diffractometer equipped with a Cu target and HyPix-3000 detector. Neutron powder diffraction data were collected on the high-resolution powder diffractometer Echidna[60] with neutron wavelength of 1.541 Å. Rietveld refinements of ND patterns were conducted using the TOPAS software. Field emission scanning electron microscopy (FE-SEM) images were obtained on an AIS 2000C scanning electron microscope.

Electrochemical evaluation of cathodes

The cathode materials are mixed with a carbon additive (acetylene black), binder (KF1100, Kureha corporation), and N-Methylpyrrolidone (Sigma-Aldrich) by mortar and pestle to prepare a slurry. The ratio of active material, carbon additive, and binder is 92:1:7. The slurries are cast on the Al foil by a doctor blade and dried for 5 hours in a vacuum oven at 120 ºC. The average tap density of electrodes was c.a. 10 mg cm^{-2}. The electrodes are cut into 12 cm^2 sized rectangle shape, and pouch cells are used for the electrochemical test. 200 μL of 1.3 M $LiPF_6$ in EC:DEC (1:1 vol.%) and polypropylene separator (Celgard) was used for the cell fabrication. Galvanostatic charge-discharge tests of the cells were performed with a current density of 30 mAh g^{-1}.

Ex-situ resonant inelastic X-ray scattering (RIXS)

The O *K*-edge RIXS spectra were collected by iRIXS endstation at beamline 8.0.1 in Advanced Light Source, Lawrence Berkeley National Laboratory. A homemade transfer kit was used to transfer the species from the Ar-filled glovebox to the measurement chamber to avoid any air exposure to the samples. The RIXS spectra were continuously scanned through the O-*K* pre-edge region with the excitation energy step size of 0.2 eV and dwelling time of 90 seconds. To minimize beam damage, the specimen was repeatedly moved up and down by 0.5 mm during measurement, and it was confirmed that the spectrum was well averaged due to the long dwelling time. The collected spectra were fabricated to 2D RIXS maps as functions of emission and excitation energies. Further processing, including normalization, cosmic ray removal, etc., has been conducted for the 2D map as used in our previous work. [12]

X-ray Absorption Spectroscopy (XAS)

The Ni and Co L_3-edge XAS spectra were collected by iRIXS endstation at beamline 8.0.1 in Advanced Light Source, Lawrence Berkeley National Laboratory. The species are transferred in the same way as used for the RIXS experiments. The iRIXS endstation has two channels to collect the total fluorescence yield (TFY) and total electron yield (TEY), and both TFY and TEY signals are collected simultaneously.

Inverse partial fluorescence yield (iPFY)

Mn-L_3 iPFY was extracted through the formula iPFY = a/PFY_O, where a is a normalization coefficient, PFY_O is extracted by integrating the fluorescence intensity within the O-*K* emission energy range (490 to 530 eV) on the Mn-

L_3 mRIXS. Mn-L_3 iPFY was used in this work instead of TFY to avoid the distortion observed in the conventional TFY caused by emission signals from oxygen.

Operando electrochemical mass spectroscopy (OEMS)

Electrode preparation for OEMS experiments

NCM electrodes for *operando* gas measurements were prepared by grinding NCM, acetylene black (Alfa Aesar, 50 % compressed, S.A. 75 m^2 g^{-1}, bulk density 80–120 g L^{-1}, 99.9%+) and polyvinylidene difluoride (Solvay, Solef 6010/1001) in an 85:8:7 mass ratio with an agate mortar and pestle inside an argon-filled glovebox (O_2 and H_2O <1 ppm). N-methyl-2-pyrrolidone (NMP, 99.5%, anhydrous, Sigma-Aldrich) was added to form a slurry, which was drop-cast onto stainless-steel mesh discs (12 mm ⌀; 1.13 cm^2). The electrodes were dried first at 60 °C for 2 hours and then at 120 °C under vacuum overnight. The active material loading was 3.5 – 4.5 mg cm^{-2}.

OEMS experiments

For the operando gas measurements, a custom-built setup and gas-tight cell, which have been described in detail in previous publications, [61-63] were used.

Custom Swagelok cells were assembled inside an argon-filled glovebox as follows: a lithium foil disc (12 mm ⌀), a quartz microfiber separator (Whatman, QM-A; 12.7 mm ⌀) wetted with 80 µL of electrolyte solution, an NMC electrode on stainless-steel mesh current collector (12 mm ⌀), a stainless-steel mesh disc (12 mm ⌀) and a stainless-steel ring spacer (12 mm ⌀) were compressed inside a modified Swagelok cell. The spacer ring creates a headspace (~100 µL) for gases to accumulate during battery operation. 1.5 M $LiPF_6$ in EC was chosen as the electrolyte solution for its low vapor pressure, thus contributing a smaller background signal in the mass spectra compared to electrolyte solutions containing linear alkyl carbonates.

After assembly, the NMC/Li cells were connected to the DEMS equipment and the headspace of the cell was filled with a positive argon pressure (~1.45 bar). During the electrochemical measurements, the cell headspace was flushed with 500 µL of argon by the DEMS instrument every 10 minutes, and any accumulated gases were swept to the mass spectrometer chamber for analysis. The mass spectrometer was calibrated for O_2 (research grade, Linde) and CO_2 (> 99.9%, Linde), allowing for the conversion of the ion current to partial pressure for O_2 and CO_2, which could then be used to quantify the gas formation using the ideal gas law (temperature and volume are known).

Electrochemical measurements were performed at 25 °C using a Biologic VSP potentiostat/galvanostat instrument running EC-lab software. After a 2-hour OCV period to establish a baseline value for all mass traces, the NMC/Li cells were cycled between 4.8 – 3.0 V_{cell}. Charging was performed at C/10 in constant current-constant voltage (CCCV) mode with a current limitation corresponding to C/100, and discharging was performed at C/5 in constant current (CC) mode.

References

1 Goodenough, J. B. & Kim, Y. Challenges for Rechargeable Li Batteries. *Chem. Mater.* 22, 587-603 (2009).

2 Ryu, H.-H., Namkoong, B., Kim, J.-H., Belharouak, I., Yoon, C. S. & Sun, Y.-K. Capacity Fading Mechanisms in Ni-Rich Single-Crystal NCM Cathodes. *ACS Energy Lett.* 6, 2726-2734 (2021).

3 Lee, W., Muhammad, S., Kim, T., Kim, H., Lee, E., Jeong, M., Son, S., Ryou, J.-H. & Yoon, W.-S. New Insight into Ni-Rich Layered Structure for Next-Generation Li Rechargeable Batteries. *Adv. Energy Mater.* 8, 1701788-1701799 (2018).

4 Liu, J., Du, Z., Wang, X., Tan, S., Wu, X., Geng, L., Song, B., Chien, P.-H., Everett, S. M. & Hu, E. Anionic redox induced anomalous structural transition in Ni-rich cathodes. *Energy Envrion. Sci.* 14, 6441-6454 (2021).

5 Zhang, S. S. Problems and their origins of Ni-rich layered oxide cathode materials. *Energy Storage Mater.* 24, 247-254 (2020).

6 Robert, R., Bünzli, C., Berg, E. J. & Novák, P. Activation Mechanism of $LiNi_{0.80}Co_{0.15}Al_{0.05}O_2$: Surface and Bulk Operando Electrochemical, Differential Electrochemical Mass Spectrometry, and X-ray Diffraction Analyses. *Chem. Mater.* 27, 526-536 (2015).

7 Jung, R., Metzger, M., Maglia, F., Stinner, C. & Gasteiger, H. A. Oxygen Release and Its Effect on the Cycling Stability of $LiNi_xMn_yCo_zO_2$(NMC) Cathode Materials for Li-Ion Batteries. *J. Electrochem. Soc.* 164, A1361-A1377 (2017).

8 de Biasi, L., Schiele, A., Roca-Ayats, M., Garcia, G., Brezesinski, T., Hartmann, P. & Janek, J. Phase Transformation Behavior and Stability of $LiNiO_2$ Cathode Material for Li-Ion Batteries Obtained from In Situ Gas Analysis and Operando X-Ray Diffraction. *ChemSusChem* 12, 2240-2250 (2019).

9 Ryu, H.-H., Park, K.-J., Yoon, C. S. & Sun, Y.-K. Capacity Fading of Ni-Rich $Li[Ni_xCo_yMn_{1-x-y}]O_2$ ($0.6 \leq x \leq 0.95$) Cathodes for High-Energy-Density Lithium-Ion Batteries: Bulk or Surface Degradation? *Chem. Mater.* 30, 1155-1163 (2018).

10 Min, S. H., Jo, M. R., Choi, S.-Y., Kim, Y.-I. & Kang, Y.-M. A Layer-Structured Electrode Material Reformed by a PO_4-O_2 Hybrid Framework toward Enhanced Lithium Storage and Stability. *Adv. Energy Mater.* 6, 1501717-1501729 (2016).

11 Chu, Y., Lai, A., Pan, Q., Zheng, F., Huang, Y., Wang, H. & Li, Q. Construction of internal electric field to suppress oxygen evolution of Ni-rich cathode materials at a high cutoff voltage. *J. Energy Chem.* 73, 114-125 (2022).

12 Lee, G.-H., Wu, J., Kim, D., Cho, K., Cho, M., Yang, W. & Kang, Y. M. Reversible Anionic Redox Activities in Conventional $LiNi_{1/3}Co_{1/3}Mn_{1/3}O_2$ Cathodes. *Angew. Chem. Int. Ed.* 59, 8681-8688 (2020).

13 Dai, K., Mao, J., Zhuo, Z., Feng, Y., Mao, W., Ai, G., Pan, F., Chuang, Y.-d., Liu, G. & Yang, W. Negligible voltage hysteresis with strong anionic redox in conventional battery electrode. *Nano Energy* 74, 104831-104837 (2020).

14 Tsuchimoto, A., Shi, X. M., Kawai, K., Mortemard de Boisse, B., Kikkawa, J., Asakura, D., Okubo, M. & Yamada, A. Nonpolarizing oxygen-redox capacity without O-O dimerization in $Na_2Mn_3O_7$. *Nat. Commun.* 12, 631-637 (2021).

15 Zhang, J.-N., Li, Q., Ouyang, C., Yu, X., Ge, M., Huang, X., Hu, E., Ma, C., Li, S., Xiao, R., Yang, W., Chu, Y., Liu, Y., Yu, H., Yang, X.-Q., Huang, X., Chen, L. & Li, H. Trace doping of multiple elements enables stable battery cycling of $LiCoO_2$ at 4.6 V. *Nat. Energy* 4, 594-603 (2019).

16 Li, N., Sallis, S., Papp, J. K., Wei, J., McCloskey, B. D., Yang, W. & Tong, W. Unraveling the Cationic and Anionic Redox Reactions in a Conventional Layered Oxide Cathode. *ACS Energy Lett.* 4, 2836-2842 (2019).

17 Hu, E., Li, Q., Wang, X., Meng, F., Liu, J., Zhang, J.-N., Page, K., Xu, W., Gu, L., Xiao, R., Li, H., Huang, X., Chen, L., Yang, W., Yu, X. & Yang, X.-Q. Oxygen-redox reactions in $LiCoO_2$ cathode without O–O bonding during charge-discharge. *Joule* 5, 720-736 (2021).

18 Lebens-Higgins, Z. W., Faenza, N. V., Radin, M. D., Liu, H., Sallis, S., Rana, J., Vinckeviciute, J., Reeves, P. J., Zuba, M. J., Badway, F., Pereira, N., Chapman, K. W., Lee, T.-L., Wu, T., Grey, C. P., Melot, B. C., Van Der Ven, A., Amatucci, G. G., Yang, W. & Piper, L. F. J. Revisiting the charge compensation mechanisms in $LiNi_{0.8}Co_{0.2-y}Al_yO_2$ systems. *Mater. Horizons* 6, 2112-2123 (2019).

19 Liu, X., Xu, G.-L., Kolluru, V. S. C., Zhao, C., Li, Q., Zhou, X., Liu, Y., Yin, L., Zhuo, Z., Daali, A., Fan, J.-J., Liu, W., Ren, Y., Xu, W., Deng, J., Hwang, I., Ren, D., Feng, X., Sun, C., Huang, L., Zhou, T., Du, M., Chen, Z., Sun, S.-G., Chan, M. K. Y., Yang, W., Ouyang, M. & Amine, K. Origin and regulation of oxygen redox instability in high-voltage battery cathodes. *Nat. Energy* 7, 808-817 (2022).

20 Kang, S., Choi, D., Lee, H., Choi, B. & Kang, Y. M. A Mechanistic Insight into the Oxygen Redox of Li-Rich Layered Cathodes and their Related Electronic/Atomic Behaviors Upon Cycling. *Adv. Mater.* 35, e2211965-2211986 (2023).

21 House, R. A., Maitra, U., Jin, L., Lozano, J. G., Somerville, J. W., Rees, N. H., Naylor, A. J., Duda, L. C., Massel, F., Chadwick, A. V., Ramos, S., Pickup, D. M., McNally, D. E., Lu, X., Schmitt, T., Roberts, M. R. & Bruce, P. G. What Triggers Oxygen Loss in Oxygen Redox Cathode Materials? *Chem. Mater.* 31, 3293-3300 (2019).

22 Li, N., Sallis, S., Papp, J. K., McCloskey, B. D., Yang, W. & Tong, W. Correlating the phase evolution and anionic redox in Co-Free Ni-Rich layered oxide cathodes. *Nano Energy* 78, 105365-105375 (2020).

23 Kaufman, L. A. & McCloskey, B. D. Surface Lithium Carbonate Influences Electrolyte Degradation via Reactive Oxygen Attack in Lithium-Excess Cathode Materials. *Chem. Mater.* 33, 4170-4176 (2021).

24 Eum, D., Kim, B., Kim, S. J., Park, H., Wu, J., Cho, S. P., Yoon, G., Lee, M. H., Jung, S. K., Yang, W., Seong, W. M., Ku, K., Tamwattana, O., Park, S. K., Hwang, I. & Kang, K. Voltage decay and redox asymmetry mitigation by reversible cation migration in lithium-rich layered oxide electrodes. *Nat. Mater.* 19, 419-427 (2020).

25 Gent, W. E., Abate, I. I., Yang, W., Nazar, L. F. & Chueh, W. C. Design Rules for High-Valent Redox in Intercalation Electrodes. *Joule* 4, 1369-1397 (2020).

26 Strehle, B., Kleiner, K., Jung, R., Chesneau, F., Mendez, M., Gasteiger, H. A. & Piana, M. The Role of Oxygen Release from Li- and Mn-Rich Layered Oxides during the First Cycles Investigated by On-Line Electrochemical Mass Spectrometry. *J. Electrochem. Soc.* 164, A400-A406 (2017).

27 Rinkel, B. L. D., Vivek, J. P., Garcia-Araez, N. & Grey, C. P. Two electrolyte decomposition pathways at nickel-rich cathode surfaces in lithium-ion batteries. *Energy Environ Sci* 15, 3416-3438 (2022).

28 Renfrew, S. E., Kaufman, L. A. & McCloskey, B. D. Altering Surface Contaminants and Defects Influences the First-Cycle Outgassing and Irreversible Transformations of $LiNi_{0.6}Mn_{0.2}Co_{0.2}O_2$. *ACS Appl. Mater. Interfaces* 11, 34913-34921 (2019).

29 Wu, J., Li, Q., Sallis, S., Zhuo, Z., Gent, W. E., Chueh, W. C., Yan, S., Chuang, Y.-d. & Yang, W. Fingerprint Oxygen Redox Reactions in Batteries through High-Efficiency Mapping of Resonant Inelastic X-ray Scattering. *Condens. Matter* 4 (2019).

30 House, R. A., Maitra, U., Perez-Osorio, M. A., Lozano, J. G., Jin, L., Somerville, J. W., Duda, L. C., Nag, A., Walters, A., Zhou, K. J., Roberts, M. R. & Bruce, P. G. Superstructure control of first-cycle voltage hysteresis in oxygen-redox cathodes. *Nature* 577, 502-508 (2020).

31 Lee, G. H., Lau, V. W. H., Yang, W. & Kang, Y. M. Utilizing Oxygen Redox in Layered Cathode Materials from Multiscale Perspective. *Adv. Energy Mater.* 11, 2003227-2003261 (2021).

32 Yang, W. & Devereaux, T. P. Anionic and cationic redox and interfaces in batteries: Advances from soft X-ray absorption spectroscopy to resonant inelastic scattering. *J. Power. Sources* 389, 188-197 (2018).

33 Sun, H. H., Kim, U. H., Park, J. H., Park, S. W., Seo, D. H., Heller, A., Mullins, C. B., Yoon, C. S. & Sun, Y. K. Transition metal-doped Ni-rich layered cathode materials for durable Li-ion batteries. *Nat. Commun.* 12, 6552-6561 (2021).

34 Cheng, C., Ding, M., Yan, T., Jiang, J., Mao, J., Feng, X., Chan, T. S., Li, N. & Zhang, L. Anionic Redox Activities Boosted by Aluminum Doping in Layered Sodium-Ion Battery Electrode. *Small Methods* 6, e2101524-e2101534 (2022).

35 Dianat, A., Seriani, N., Bobeth, M. & Cuniberti, G. Effects of Al-doping on the properties of Li–Mn–Ni–O cathode materials for Li-ion batteries: an ab initio study. *J. Mater. Chem. A* 1, 9273-9280 (2013).

36 Dixit, M., Markovsky, B., Aurbach, D. & Major, D. T. Unraveling the Effects of Al Doping on the Electrochemical Properties of $LiNi_{0.5}Co_{0.2}Mn_{0.3}O_2$ Using First Principles. *J. Electrochem. Soc.* 164, A6359-A6365 (2017).

37 Ben Yahia, M., Vergnet, J., Saubanere, M. & Doublet, M. L. Unified picture of anionic redox in Li/Na-ion batteries. *Nat. Mater.* 18, 496-502 (2019).

38 Zhuo, Z., Liu, Y. S., Guo, J., Chuang, Y. D., Pan, F. & Yang, W. Full Energy Range Resonant Inelastic X-ray Scattering of O_2 and CO_2: Direct Comparison with Oxygen Redox State in Batteries. *J. Phys. Chem. Lett.* 11, 2618-2623 (2020).

39 Zhuo, Z., Pemmaraju, C. D., Vinson, J., Jia, C., Moritz, B., Lee, I., Sallies, S., Li, Q., Wu, J., Dai, K., Chuang, Y. D., Hussain, Z., Pan, F., Devereaux, T. P. & Yang, W. Spectroscopic Signature of Oxidized Oxygen States in Peroxides. *J. Phys. Chem. Lett.* 9, 6378-6384 (2018).

40 Risch, M., Stoerzinger, K. A., Han, B., Regier, T. Z., Peak, D., Sayed, S. Y., Wei, C., Xu, Z. & Shao-Horn, Y. Redox Processes of Manganese Oxide in Catalyzing Oxygen Evolution and Reduction: An in Situ Soft X-

ray Absorption Spectroscopy Study. *J. Phys. Chem. C* 121, 17682-17692 (2017).

41 Tesch, M. F., Bonke, S. A., Jones, T. E., Shaker, M. N., Xiao, J., Skorupska, K., Mom, R., Melder, J., Kurz, P., Knop-Gericke, A., Schlogl, R., Hocking, R. K. & Simonov, A. N. Evolution of Oxygen-Metal Electron Transfer and Metal Electronic States During Manganese Oxide Catalyzed Water Oxidation Revealed with In Situ Soft X-Ray Spectroscopy. *Angew. Chem. Int. Ed.* 58, 3426-3432 (2019).

42 Fang, L., Zhou, L., Park, M., Han, D., Lee, G. H., Kang, S., Lee, S., Chen, M., Hu, Z., Zhang, K., Nam, K. W. & Kang, Y. M. Hysteresis Induced by Incomplete Cationic Redox in Li-Rich 3d-Transition-Metal Layered Oxides Cathodes. *Adv. Sci.* 9, e2201896-2201905 (2022).

43 Zhang, J., Kim, J. B., Zhang, J., Lee, G. H., Chen, M., Lau, V. W., Zhang, K., Lee, S., Chen, C. L., Jeon, T. Y., Kwon, Y. W. & Kang, Y. M. Regulating Pseudo-Jahn-Teller Effect and Superstructure in Layered Cathode Materials for Reversible Alkali-Ion Intercalation. *J. Am. Chem. Soc.* 144, 7929-7938 (2022).

44 Fang, L., Han, D., Kang, S., Heo, U.-S., Nam, K.-W. & Kang, Y.-M. Non-monotonic first-cycle irreversible capacity governed by delithiation depth in Li-rich layered cathodes. *Energy Envrion. Sci.* 16, 3053-3062 (2023).

45 Qiao, R., Wray, L. A., Kim, J.-H., Pieczonka, N. P. W., Harris, S. J. & Yang, W. Direct Experimental Probe of the Ni(II)/Ni(III)/Ni(IV) Redox Evolution in $LiNi_{0.5}Mn_{1.5}O_4$ Electrodes. *J. Phys. Chem. C* 119, 27228-27233 (2015).

46 Liu, X., Liu, J., Qiao, R., Yu, Y., Li, H., Suo, L., Hu, Y. S., Chuang, Y. D., Shu, G., Chou, F., Weng, T. C., Nordlund, D., Sokaras, D., Wang, Y. J., Lin, H., Barbiellini, B., Bansil, A., Song, X., Liu, Z., Yan, S., Liu, G., Qiao, S., Richardson, T. J., Prendergast, D., Hussain, Z., de Groot, F. M. & Yang, W. Phase transformation and lithiation effect on electronic structure of Li_xFePO_4: an in-depth study by soft X-ray and simulations. *J. Am. Chem. Soc.* 134, 13708-13715 (2012).

47 Qiao, R., Wang, Y., Olalde-Velasco, P., Li, H., Hu, Y.-S. & Yang, W. Direct evidence of gradient Mn(II) evolution at charged states in $LiNi_{0.5}Mn_{1.5}O_4$ electrodes with capacity fading. *J. Power. Sources* 273, 1120-1126 (2015).

48 Yang, F., Feng, X., Liu, Y. S., Kao, L. C., Glans, P. A., Yang, W. & Guo, J. In Situ/Operando (Soft) X-ray Spectroscopy Study of Beyond Lithium-ion Batteries. *Energy Environ. Mater.* 4, 139-157 (2021).

49 Singh, J. P., Park, J. Y., Chae, K. H., Ahn, D. & Lee, S. Soft X-ray Absorption Spectroscopic Investigation of $Li(Ni_{0.8}Co_{0.1}Mn_{0.1})O_2$ Cathode Materials. *Nanomater.* 10 (2020).

50 Tallman, K. R., Wheeler, G. P., Kern, C. J., Stavitski, E., Tong, X., Takeuchi, K. J., Marschilok, A. C., Bock, D. C. & Takeuchi, E. S. Nickel-rich Nickel Manganese Cobalt (NMC622) Cathode Lithiation Mechanism and Extended Cycling Effects Using Operando X-ray Absorption Spectroscopy. *J. Phys. Chem. C* 125, 58-73 (2020).

51 Liang, C., Jiang, L., Wei, Z., Zhang, W., Wang, Q. & Sun, J. Insight into the structural evolution and thermal behavior of $LiNi_{0.8}Co_{0.1}Mn_{0.1}O_2$ cathode under deep charge. *J. Energy Chem.* 65, 424-432 (2022).

52 Dai, H., Gomes, L., Maxwell, D., Zamani, S., Yang, K., Atienza, D., Dale, N. & Mukerjee, S. Exploring the Role of an Electrolyte Additive in Suppressing Surface Reconstruction of a Ni-Rich NMC Cathode at Ultrahigh Voltage via Enhanced In Situ and Operando Characterization Methods. *ACS Appl. Mater. Interfaces* 16, 8639-8654 (2024).

53 Flores, E., Novák, P., Aschauer, U. & Berg, E. J. Cation Ordering and Redox Chemistry of Layered Ni-Rich $Li_xNi_{1-2y}Co_yMn_yO_2$: An Operando Raman Spectroscopy Study. *Chem. Mater.* 32, 186-194 (2019).

54 Oswald, S. & Gasteiger, H. A. The Structural Stability Limit of Layered Lithium Transition Metal Oxides Due to Oxygen Release at High State of Charge and Its Dependence on the Nickel Content. *J. Electrochem. Soc.* 170, 030506-030522 (2023).

55 House, R. A., Marie, J.-J., Pérez-Osorio, M. A., Rees, G. J., Boivin, E. & Bruce, P. G. The role of O_2 in O-redox cathodes for Li-ion batteries. *Nat. Energy* 6, 781-789 (2021).

56 Saubanère, M., McCalla, E., Tarascon, J. M. & Doublet, M. L. The intriguing question of anionic redox in high-energy density cathodes for Li-ion batteries. *Energy Envrion. Sci.* 9, 984-991 (2016).

57 Zhang, S. S. Understanding of performance degradation of $LiNi_{0.80}Co_{0.10}Mn_{0.10}O_2$ cathode material operating at high potentials. *J. Energy Chem.* 41, 135-141 (2020).

Supporting information

Oxygen Activities Governing Structural Reversibility in Industrial Ni-Rich Layered Cathodes

Table of contents

Table S1. The elemental composition of NR-NCMs and NR-NCMAs analyzed by ICP-OES

Samples	Elemental composition				
	Li	Ni	Co	Mn	Al
622	0.99	0.62	0.19	0.19	N/A
712	1.00	0.72	0.09	0.19	N/A
712-Al	0.98	0.73	0.09	0.19	0.007
811	0.97	0.87	0.1	0.06	N/A
811-Al	0.98	0.89	0.05	0.07	0.019

*Similar levels of impurities (> 2000 ppm) like Zr and B are detected through all samples

Table S2. Rietveld refinement results of neutron diffraction patterns of NR-NCMs and NR-NCMAs

NCM622 (space group: R$\bar{3}$m)

R_{wp} = 3.67 %, R_e = 1.49 %, R_p = 2.99 %, S (= R_{wp}/R_e) = 2.46
Lattice parameters: a = b = 2.86797(15) Å, c = 14.2172(10) Å, α = β= 90°, γ= 120°

Atom	Site	x	y	z	Occupancy	B_{iso} (Å)
Ni	3a	0	0	0	0.576(2)	0
Co	3a	0	0	0	0.210(6)	0
Mn	3a	0	0	0	0.194(10)	0
Li	3a	0	0	0	0.020(12)	0
Li2	3b	0	0	0.5	1	0
O	6c	0	0	0.25881(10)	1	0

NCM712 (space group: R$\bar{3}$m)

R_{wp} = 2.90 %, R_e = 2.24 %, R_p = 2.34 %, S (= R_{wp}/R_e) = 1.30
Lattice parameters: a = b = 2.87326(3) Å, c = 14.22389(19) Å, α = β= 90°, γ= 120°

Atom	Site	x	y	z	Occupancy	B_{iso} (Å)
Ni	3a	0	0	0	0.646(2)	0
Co	3a	0	0	0	0.102(6)	0
Mn	3a	0	0	0	0.161(10)	0
Li	3a	0	0	0	0.091(12)	0
Li2	3b	0	0	0.5	0.956	0
Ni2	3b	0	0	0.5	0.044(12)	
O	6c	0	0	0.25881(10)	1	0

NCM712-Al (space group: R$\bar{3}$m)

R_{wp} = 3.86 %, R_e = 1.47 %, R_p = 3.17 %, S (= R_{wp}/R_e) = 2.63
Lattice parameters: a = b = 2.86568(19) Å, c = 14.1868(10) Å, α = β= 90°, γ= 120°

Atom	Site	x	y	z	Occupancy	B_{iso} (Å)
Ni	3a	0	0	0	0.671(1)	0
Co	3a	0	0	0	0.0787(9)	0
Mn	3a	0	0	0	0.2483(2)	0
Li	3a	0	0	0	0.0015(15)	0
Li2	3b	0	0	0.5	1	0
O	6c	0	0	0.25869(12)	1	0

NCM811 (space group: R$\bar{3}$m)

R_{wp} = 4.66 %, R_e = 1.31 %, R_p = 3.77 %, S (= R_{wp}/R_e) = 3.56
Lattice parameters: a = b = 2.86320(20) Å, c = 14.1526(11) Å, α = β= 90°, γ= 120°

Atom	Site	x	y	z	Occupancy	B_{iso} (Å)
Ni	3a	0	0	0	0.804(2)	0
Co	3a	0	0	0	0.152(5)	0
Mn	3a	0	0	0	0.044(5)	0
Li	3a	0	0	0	0	0
Li2	3b	0	0	0.5	0.981(5)	0
Ni2	3b	0	0	0.5	0.019(5)	0
O	6c	0	0	0.25881(10)	1	0

NCM811-Al (space group: R$\bar{3}$m)						
R_{wp} = 3.92 %, R_e = 1.59 %, R_p = 3.10 %, S (= R_{wp}/R_e) = 2.47 Lattice parameters: a = b = 2.86973(0) Å, c = 14.22726(0) Å, α = β= 90°, γ= 120°						
Atom	Site	x	y	z	Occupancy	B_{iso} (Å)
Ni	3a	0	0	0	0.788(4)	0
Co	3a	0	0	0	0.030(20)	0
Mn	3a	0	0	0	0.093(14)	0
Al	3a	0	0	0	0.0090(12)	0
Li2	3b	0	0	0.5	0.981(5)	0
Ni2	3b	0	0	0.5	0.019(5)	0
O	6c	0	0	0.25881(10)	1	0

Table S3. Accumulated CO_2/O_2 gas evolution during the cycling of NR-NCMs and NR-NCMAs

NCM622	O_2 (μmol g^{-1})	CO_2 (μmol g^{-1})
Cycle 1	2.0041	104.3826
Cycle 2	0.2671	68.11

NCM712	O_2 (μmol g^{-1})	CO_2 (μmol g^{-1})
Cycle 1	1.9817	113.3374
Cycle 2	0.9077	75.7738

NCM712-Al	O_2 (μmol g^{-1})	CO_2 (μmol g^{-1})
Cycle 1	1.4933	84.3190
Cycle 2	0.5023	58.1831

NCM811	O_2 (μmol g^{-1})	CO_2 (μmol g^{-1})
Cycle 1	1.5739	118.7847
Cycle 2	0.4572	72.9226

NCM811-Al	O_2 (μmol g^{-1})	CO_2 (μmol g^{-1})
Cycle 1	1.2073	81.9391
Cycle 2	0.3577	53.0161

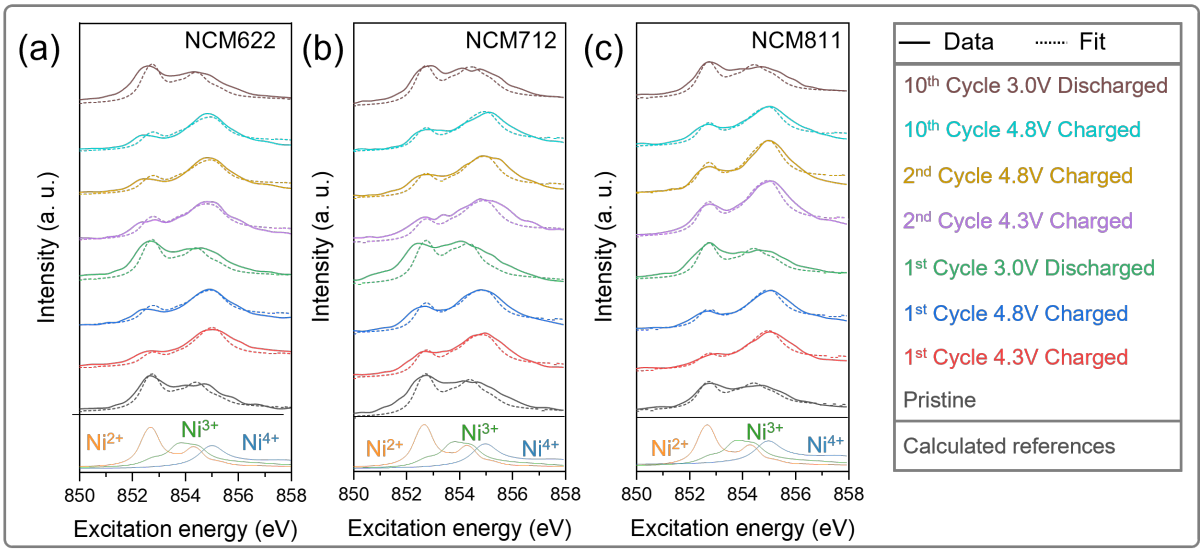

Figure S1. Ni-L_3 TFY analyses results of NR-NCMs. Soft X-ray absorption spectra of **a-c** Ni L_3-edge collected by total fluorescence yield (TFY) mode. Solid lines and dotted lines correspond to the experimental and fitted values, respectively. The fitted value is generated by the linear combination of the simulated $Ni^{2+/3+/4+}$ spectra plotted at the bottom of the boxes.

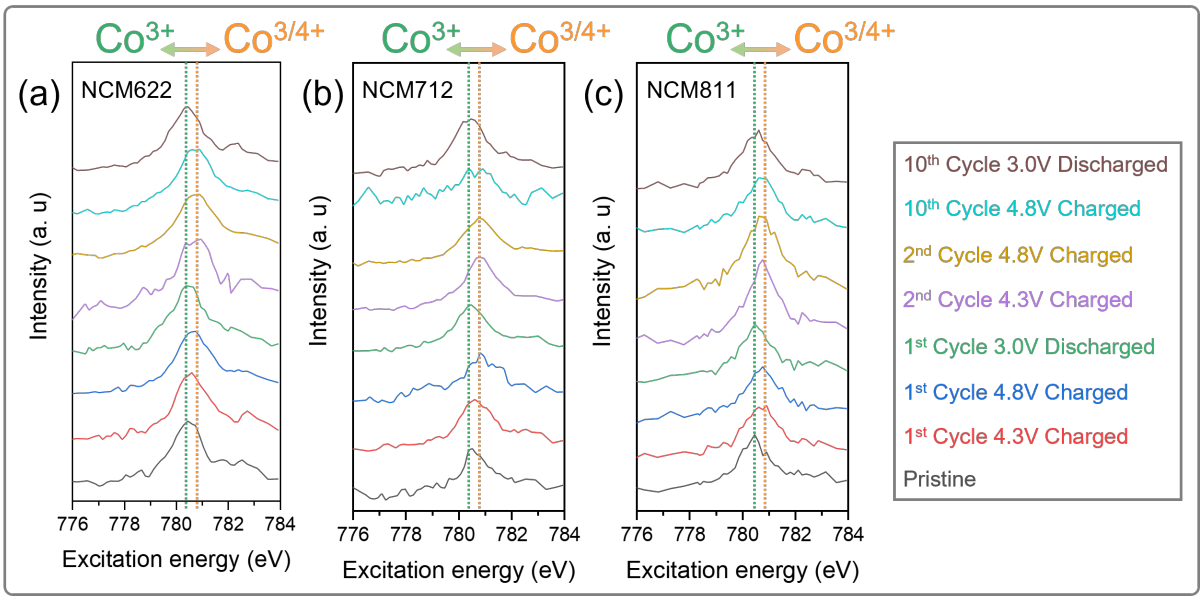

Figure S2. Co-L_3 TEY analyses results of NR-NCMs. Soft X-ray absorption spectra of **a-c** Co L_3-edge collected by total fluorescence yield (TFY) mode.

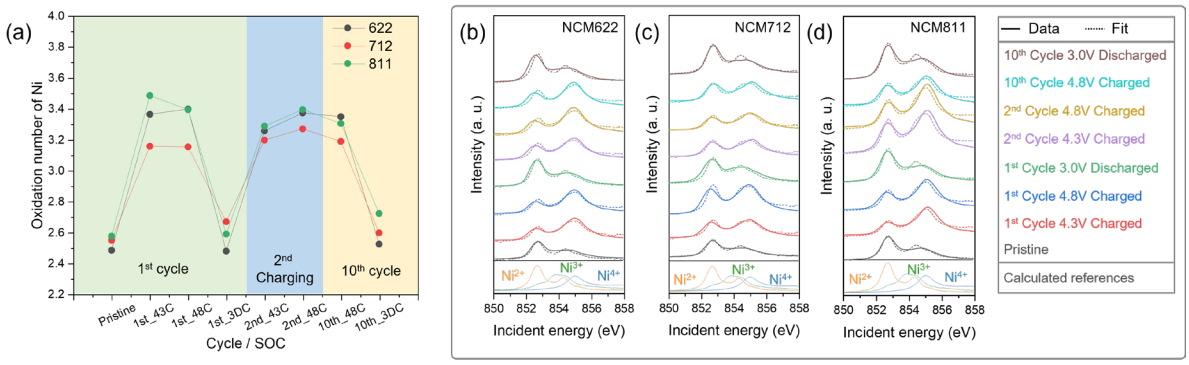

Figure S3. Ni-L_3 TEY analyses results of NR-NCMs. Soft X-ray absorption spectra of (a-d) Ni L_3-edge collected by total electron yield (TEY) mode. (a) Semi-quantitatively fitted Ni oxidation state trend extracted from Ni-L_3 spectra. (b-d) Solid lines and dotted lines correspond to the experimental and fitted values, respectively. The fitted value is generated by the linear combination of the simulated $Ni^{2+/3+/4+}$ spectra plotted at the bottom of the boxes.

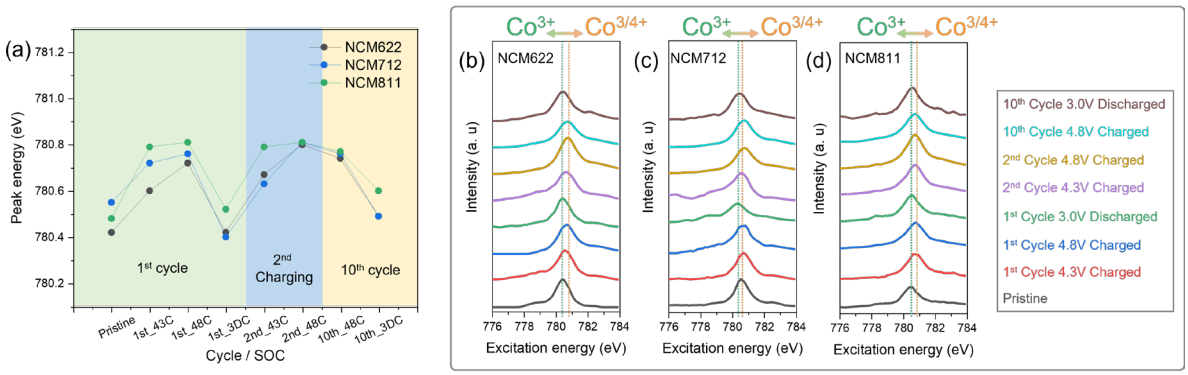

Figure S4. Co-L_3 TEY analyses results of NR-NCMs. Soft X-ray absorption spectra of (a-d) Co L_3-edge collected by total electron yield (TEY) mode. (a) Co peak energy trend during the cycling extracted from the (b-d) Co L_3-edge spectra.

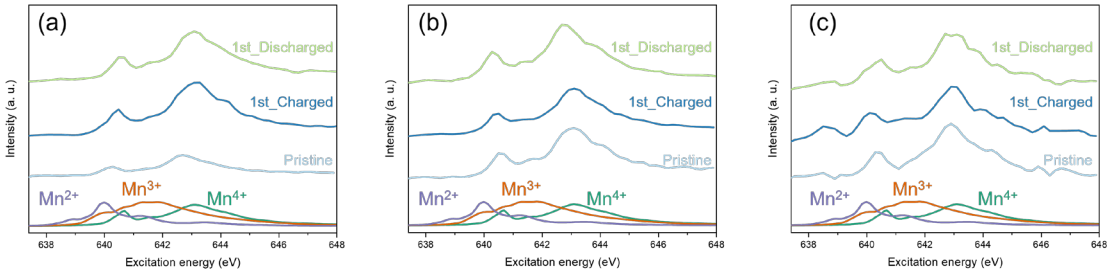

Figure S5. Mn-L_3 iPFY results of NR-NCMs. (a-c) The iPFY spectra extracted from mRIXS spectra for NCM622, NCM712, NCM811, respectively. Each panel includes the spectra at states of charge of pristine, first full charged (4.8 V) and first discharged (3.0 V). The calculated reference spectra for Mn^{2+}, Mn^{3+} and Mn^{4+} were plotted together for the comparison. [1] The similarity of all spectra with Mn^{4+} reference indicates that Mn is kept to 4+ regardless of the material and the state of charge.

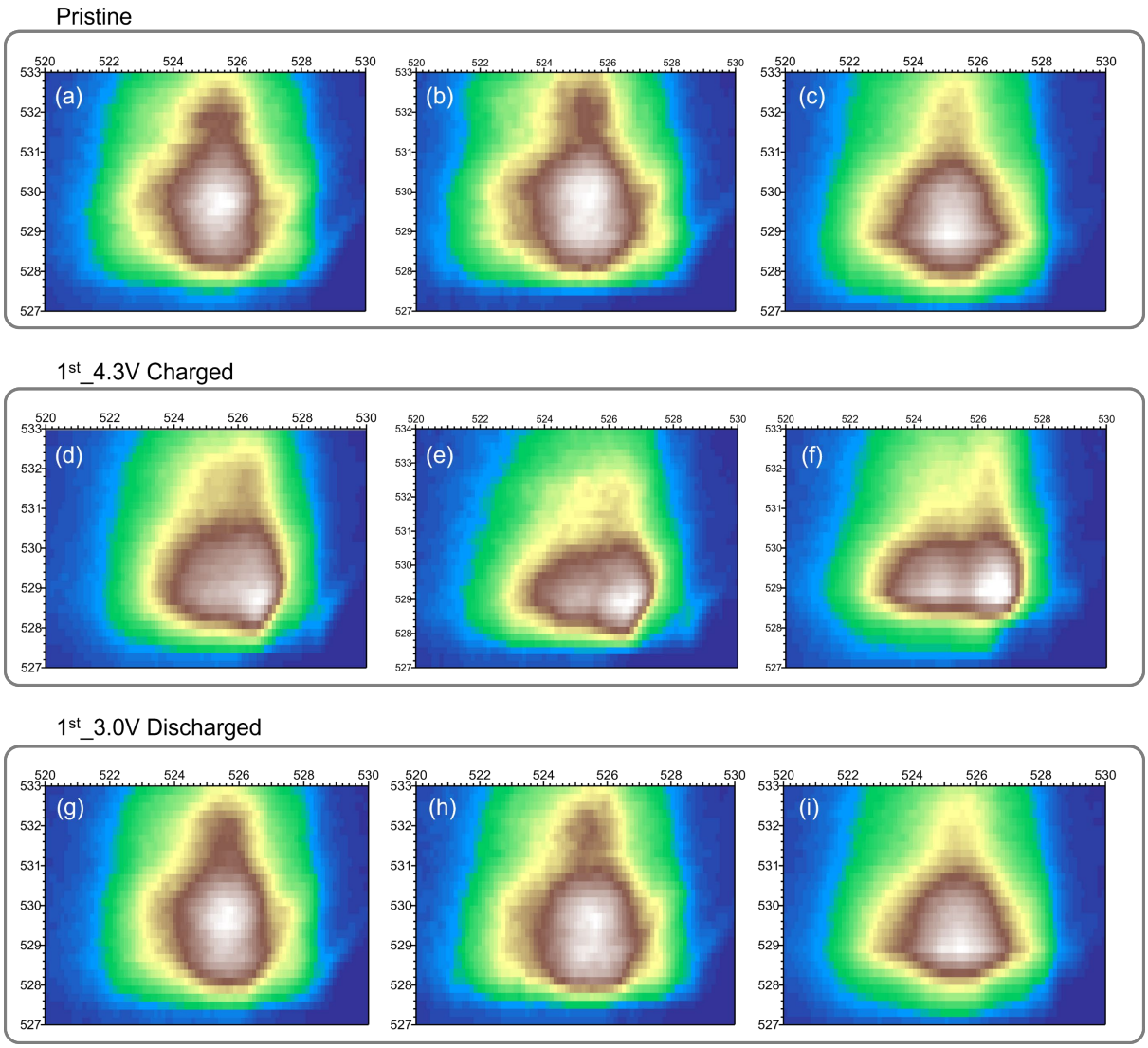

Figure S6. Additional mRIXS spectra of NR-NCMs at various states of charge: (a-c) Pristine, (d-f) first 4.3 V charged states and (g-i) first discharged states. (a, d, g) NCM 622, (b, e, h) NCM712 and (c, f, i) NCM811, respectively.

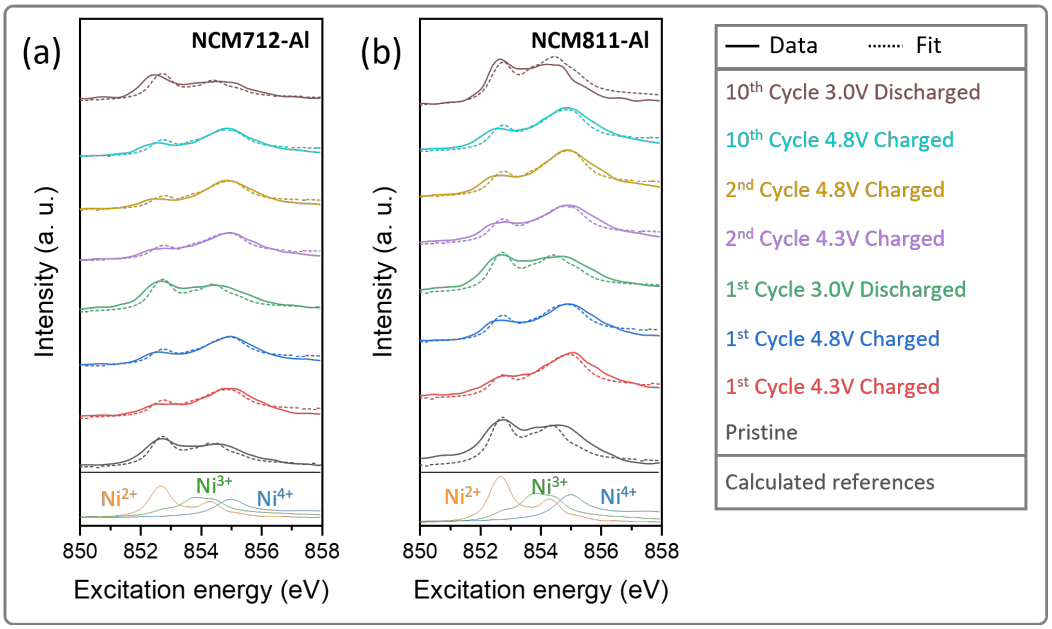

Figure S7. Ni-L_3 TFY analyses results of NR-NCMAs. Soft X-ray absorption spectra of **a, b** Ni L_3-edge collected by total fluorescence yield (TFY) mode. Solid lines and dotted lines correspond to the experimental and fitted values, respectively. The fitted value is generated by the linear combination of the simulated $Ni^{2+/3+/4+}$ spectra plotted at the bottom of the boxes.

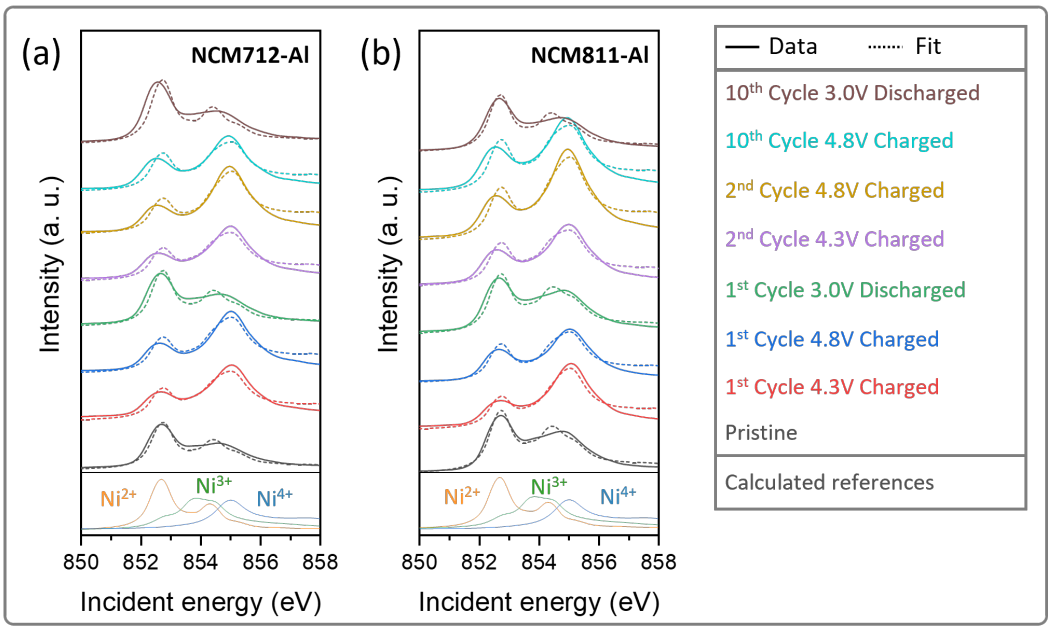

Figure S8. Ni-L_3 TEY analyses results of NR-NCMAs. Soft X-ray absorption spectra of **a, b** Ni L_3-edge collected by total fluorescence yield (TEY) mode. Solid lines and dotted lines correspond to the experimental and fitted values, respectively. The fitted value is generated by the linear combination of the simulated $Ni^{2+/3+/4+}$ spectra plotted at the bottom of the boxes.

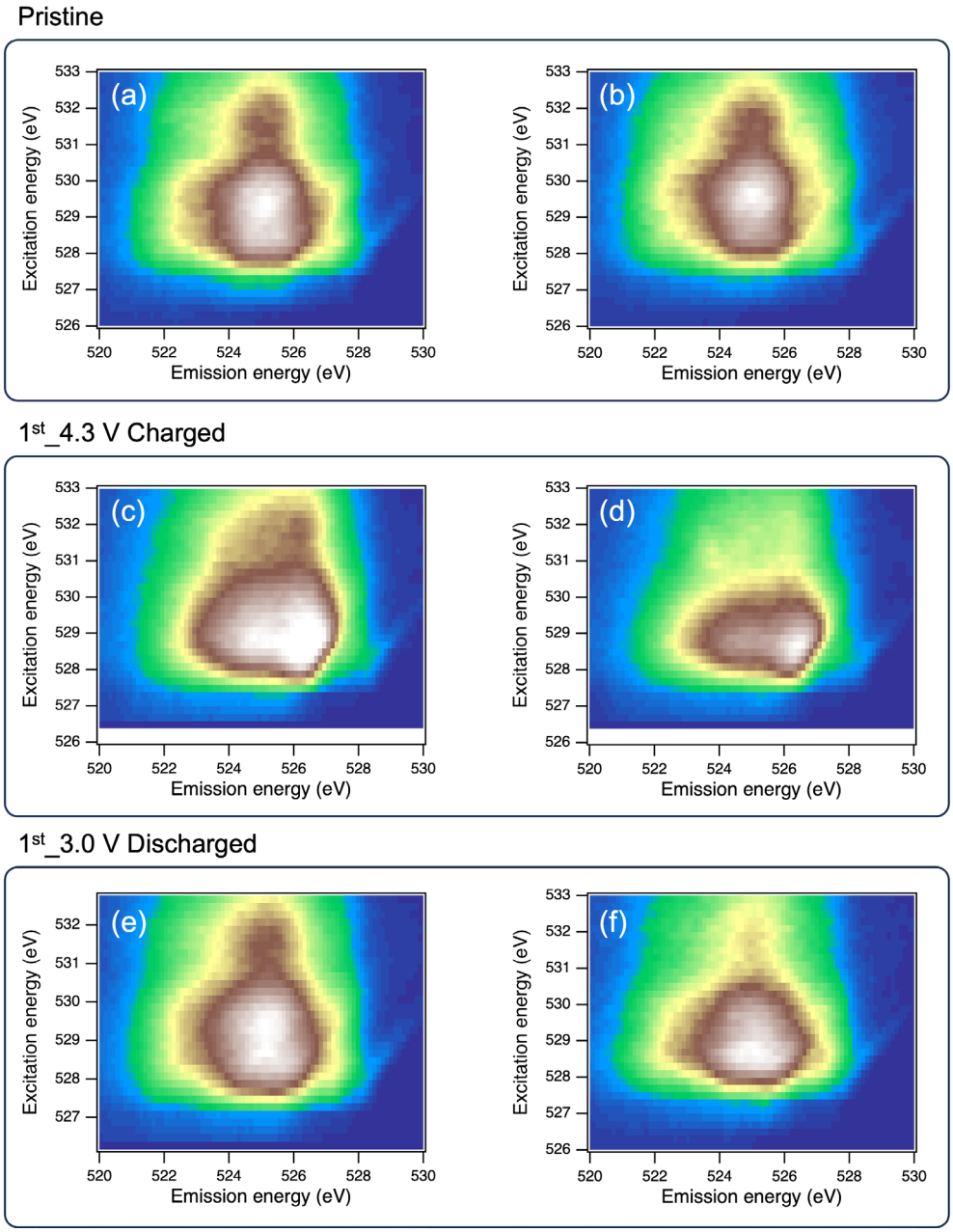

Figure S9. Additional mRIXS spectra of NR-NCMAs at various states of charge: (a, b) Pristine, (c,d) first 4.3 V charged states and (e, f) first discharged states. (a, c, e) NCM712-Al, (b, d, f) NCM811-Al, respectively.

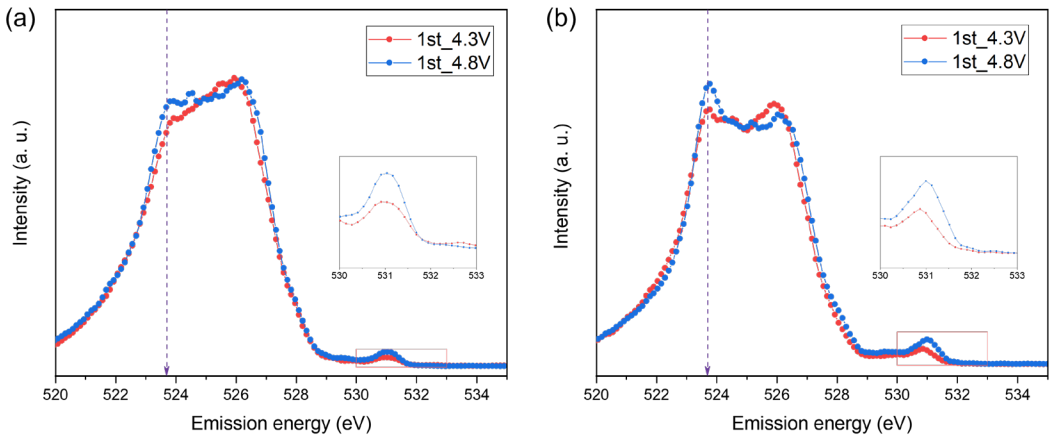

Figure S10. The summed O-*K* RIXS cuts of NR-NCMAs in the excitation energy of 530.9 – 531.3 eV at the first cycle with different voltage cut-offs. (a) NCM712-Al (b) NCM811-Al. The red box highlights the low energy emission features near the elastic lines arising from the oxygen redox.

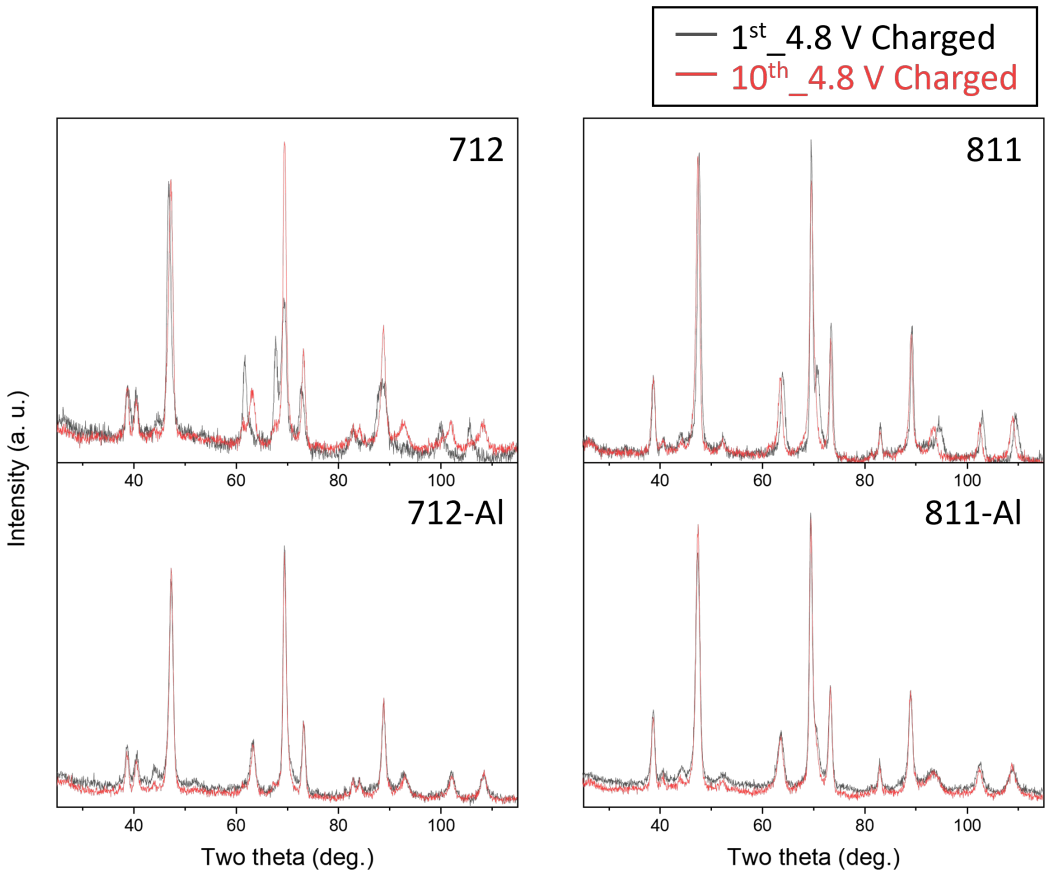

Figure S11. Full-range ND patterns of NR-NCM & NR-NCMA for the first and tenth charged states